



## Gradient Droplet Arrays by Acceleration-Mode Dip-Coating

**Mandsberg, Nikolaj K.; Shneidman, Anna V.; Jensen, Kaare H.; Taboryski, Rafael; Nielsen, Line H.; Aizenberg, Joanna; Boisen, Anja**

*Published in:*  
Advanced Materials Interfaces

*Link to article, DOI:*  
[10.1002/admi.202200667](https://doi.org/10.1002/admi.202200667)

*Publication date:*  
2022

*Document Version*  
Publisher's PDF, also known as Version of record

[Link back to DTU Orbit](#)

*Citation (APA):*  
Mandsberg, N. K., Shneidman, A. V., Jensen, K. H., Taboryski, R., Nielsen, L. H., Aizenberg, J., & Boisen, A. (2022). Gradient Droplet Arrays by Acceleration-Mode Dip-Coating. *Advanced Materials Interfaces*, 9(22), Article 2200667. <https://doi.org/10.1002/admi.202200667>

---

### General rights

Copyright and moral rights for the publications made accessible in the public portal are retained by the authors and/or other copyright owners and it is a condition of accessing publications that users recognise and abide by the legal requirements associated with these rights.

- Users may download and print one copy of any publication from the public portal for the purpose of private study or research.
- You may not further distribute the material or use it for any profit-making activity or commercial gain
- You may freely distribute the URL identifying the publication in the public portal

If you believe that this document breaches copyright please contact us providing details, and we will remove access to the work immediately and investigate your claim.

# Gradient Droplet Arrays by Acceleration-Mode Dip-Coating

Nikolaj K. Mandsberg,\* Anna V. Shneidman, Kaare H. Jensen, Rafael Taboryski, Line H. Nielsen, Joanna Aizenberg, and Anja Boisen

Droplet microarray technology is of great interest in biology and chemistry as it allows for significant reactant savings and massive parallelization of experiments. Upon scaling down the footprint of each droplet in an array, it becomes increasingly challenging to produce the array drop-by-drop. Therefore, techniques for parallelized droplet production are developed, e.g., dip-coating of biphilic substrates. However, it is in general difficult to tailor the characteristics of individual droplets, such as size and content, without updating the substrate. Here, the method of dip-coating of uniformly patterned biphilic substrates in so-called “acceleration-mode” to produce droplet arrays featuring gradients in droplet height for fixed droplet footprint is developed. The results herein present this method applied to produce drops with base diameters varying over orders of magnitude, from as high as 6 mm to as small as 50  $\mu\text{m}$ ; importantly, the experimentally measured power-law-dependency of volume on capillary-number matches analytical theory for droplet formation on heterogenous substrates though the precise quantitative values likely differ due to 2D substrate patterning. Gradient characteristics, including average droplet volume, steepness of the gradient, and its monotonicity, can all be tuned by changing the dip-coating parameters, thus providing a robust method for high-throughput screening applications and experiments.

## 1. Introduction

Parallelization of experiments is a powerful method to rapidly acquire scientific evidence, especially important for multiparameter studies. Digital droplet array technologies have become prevalent in chemistry and biochemistry, allowing for experiments to be simultaneously conducted and interrogated within a large number of droplets, each of which functions as an individual microreactor.<sup>[1–4]</sup> However, standard techniques for one-step formation of droplet arrays—such as dip-coating of biphilic substrates—do not allow for array formation with control over the individual droplets (usually, all are nearly identical in size).<sup>[5]</sup> The possibility to produce dissimilar droplets within an array, e.g., varying in size or content, would allow fast formation of microarrays for screening applications. This could be useful for combinatorial chemistry and rapid data collection for dose–response curves.

Variations in droplet volumes along a substrate have been obtained by varying the size of the hydrophilic islands on the substrate prepared for dip-coating,<sup>[6–10]</sup> but the ability to adaptively tune droplet sizes for a fixed substrate has, to our knowledge, not yet been evaluated. In the case of films, however, researchers achieved continuous films with thickness gradients by performing the dip-coating<sup>[11]</sup> or flow-coating<sup>[12]</sup> methods in acceleration-mode, i.e., accelerating the substrate during withdrawal rather than the typical constant linear velocity.

Here, we combine the parallel production of droplet arrays on biphilic substrates, consisting of hydrophilic spots in a hydrophobic matrix, with acceleration-mode dip-coating to produce height gradients across droplet arrays with fixed droplet base diameters. We show that the method of acceleration-mode dip-coating for gradient array creation is applicable across two orders of magnitude in droplet base diameters and is expected to extend even further, as well as beyond water droplets demonstrated here.

## 2. Results

### 2.1. Dip-Coating of Biphilic Substrates to Produce Droplet Arrays

Dip-coating of a biphilic substrate is a standard approach to produce droplet arrays. In general, a biphilic substrate is immersed and subsequently withdrawn from a liquid reservoir.<sup>[13]</sup> As

N. K. Mandsberg, L. H. Nielsen, A. Boisen  
The Danish National Research Foundation and Villum Foundation's  
Center for Intelligent Drug Delivery and Sensing Using Microcontainers  
and Nanomechanics (IDUN)  
Department of Health Technology  
Technical University of Denmark  
Ørstedes Plads, Kgs. Lyngby DK-2800, Denmark  
E-mail: nikoma@dtu.dk

A. V. Shneidman, J. Aizenberg  
John A. Paulson School of Engineering and Applied Sciences  
Harvard University  
Cambridge, MA 02138, USA

K. H. Jensen  
Department of Physics  
Technical University of Denmark  
Kgs. Lyngby DK-2800, Denmark

R. Taboryski  
DTU Nanolab  
National Centre for Nano Fabrication and Characterization  
Technical University of Denmark  
Kgs. Lyngby DK-2800, Denmark

 The ORCID identification number(s) for the author(s) of this article can be found under <https://doi.org/10.1002/admi.202200667>.

© 2022 The Authors. Advanced Materials Interfaces published by Wiley-VCH GmbH. This is an open access article under the terms of the Creative Commons Attribution License, which permits use, distribution and reproduction in any medium, provided the original work is properly cited.

DOI: 10.1002/admi.202200667

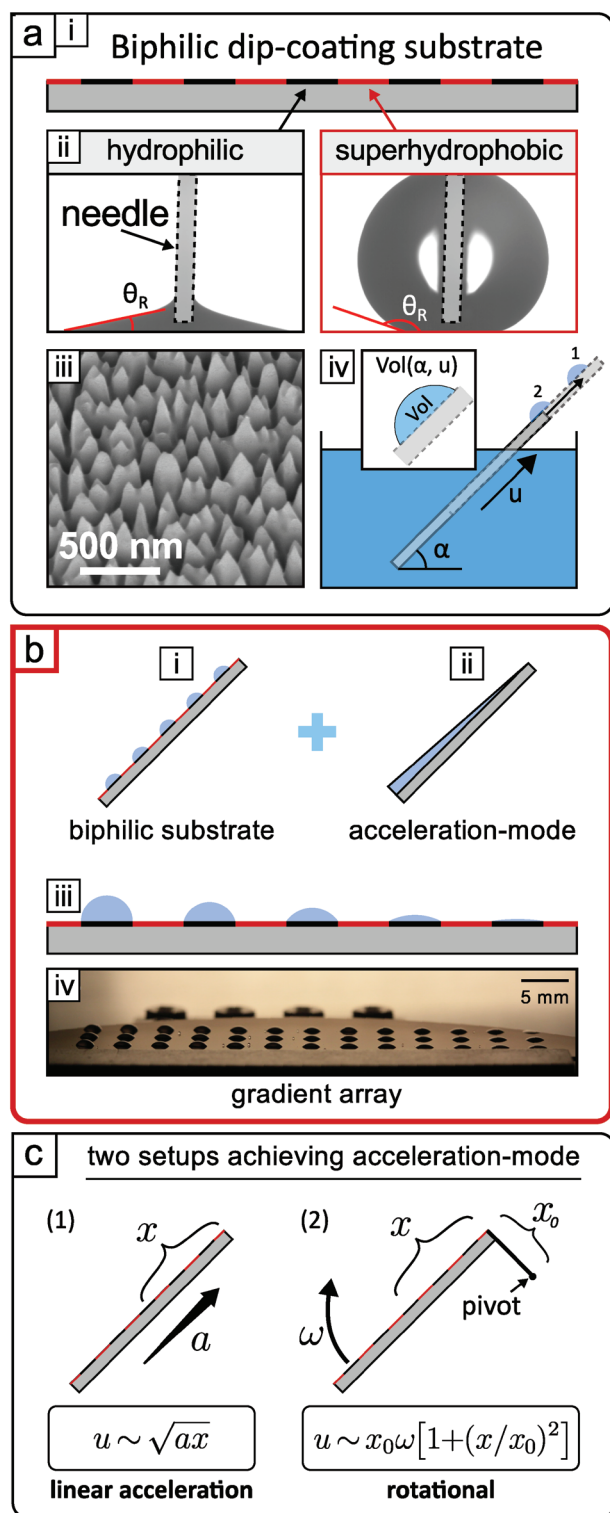


**Figure 1.** Gradient droplet arrays formed on biphilic substrates by acceleration-mode dip-coating. a) Overview of the dip-coating process to produce droplet arrays. i) The biphilic substrate is shown schematically, ii) with the receding contact angle,  $\theta_R$ , measured on the distinct regions using the needle method with inflation/deflation protocol. iii) The SEM micrograph shows the nanostructure on the substrate that enhances the wetting contrast. iv) The dip-coating process is

shown schematically in **Figure 1a-iv**, the technique entails withdrawing the substrate from a liquid reservoir at an angle,  $\alpha$ , and withdrawal speed,  $u$ . Because dip-coating is typically fully automated, it offers precise control over several parameters, such as withdrawal speed and angle between substrate and reservoir meniscus, which for millimeter-sized droplets have both been shown to affect the volume of all droplets in the array.<sup>[10]</sup> While decreasing the dip-coating angle (with respect to horizontal) increased the droplet size, the withdrawal speed had a nonmonotonic relationship with size. In the low-speed regime, droplet volume increased with speed, while it decreased in the high-speed regime where droplet heights are restricted by the viscous boundary layer.<sup>[14]</sup>

## 2.2. Chemically and Physically Functionalized Substrates

### 2.2.1. Substrate Fabrication

The biphilic substrates employed here consisted of regularly spaced identical circular hydrophilic spots in a hydrophobic matrix, with spot diameters ranging from 50  $\mu\text{m}$  to 6 mm (**Figure 1a-i** and **Figure S1**, Supporting Information). A combination of reactive ion etching (RIE), photolithography, and chemical functionalization of a silicon wafer was used to create the substrate patterning. An initial RIE step was employed to achieve nanoscale roughness across the entire surface in order to enhance the chemically induced wettability contrast, which was assessed with a sessile droplet method, as shown in **Figure 1a-ii**.<sup>[15]</sup> The chemical pattern was defined using photolithography, whereby regions masked by photoresist remained hydrophilic, while hydrophobic regions were achieved on the unmasked regions using a perfluorodecyltrichlorosilane (FDTs) coating deposited by molecular vapor deposition. The nanorough surface was observed with scanning electron microscopy (SEM), revealing a random forest of cone-like structures, with an average base diameter of  $(160 \pm 10)$  nm (calculated as the square root of the average area per cone, using 62 cones, and Poisson counting error) and an average opening angle of  $(26 \pm 7)^\circ$  (**Figure 1a-iii**). Further details of the substrate fabrication and characterization are provided in the Experimental Section and Section S1.1 in the Supporting Information.

### 2.2.2. Droplet Formation Criteria and Substrate Wetting Characterization

When dip-coating biphilic substrates, separate droplets are formed on the hydrophilic spots as the reservoir water recedes

schematically depicted;  $\alpha$ ,  $u$ , and Vol are the withdrawal angle, speed, and resulting droplet volume, respectively. b) Conceptual drawing showing how the combination of i) a biphilic substrate for droplet array creation combined with ii) the ability to produce thickness gradient by dip-coating in acceleration-mode can lead to iii) a gradient droplet array. iv) Photograph of a gradient droplet array produced in this way. c) Schematics of two different realizations of acceleration-mode dip-coating: (1) constant linear acceleration and (2) rotational dip-coating, where the withdrawal speed  $u$  varies with droplet location  $x$  as indicated. (1)  $a$  is the acceleration and (2)  $\omega$  is the angular velocity at the hinge/pivot.

**Table 1.** Wetting characteristics of biphilic substrates.

	Hydrophilic region (SiO <sub>2</sub> )		Hydrophilic region (FDTs)	
	mean	std. dev.	mean	std. dev.
<sup>a</sup> Advancing contact angle [°]	111	3	169	2
<sup>a</sup> Receding contact angle [°]	9	3	161	3
<sup>b</sup> Contact angle hysteresis [°]	102	4	8	4

<sup>a</sup>The mean and standard deviations for the advancing and receding contact angles are obtained from three repetitions of the measurement on the same substrate, i.e., a new drop is inflated/deflated on the same substrate but at a different location; <sup>b</sup>The contact angle hysteresis standard deviation is calculated using error propagation under the assumption of independent variables.

from the substrate during withdrawal. Consequently, to entrain droplets, the hydrophilic spots must pin the water while the surrounding superhydrophobic matrix preferably exhibits low contact angle hysteresis (CAH) in order to shed the water easily, as the adhesion force increases with CAH as described by the Fumridge equation.<sup>[16–18]</sup> The nanoroughness used in this work exhibits such strong pinning that the advancing contact angle was larger than 90° on native silicon oxide (i.e., within the hydrophilic spots). This extreme droplet pinning and high advancing contact angle are similar to those observed on rose petals.<sup>[19–21]</sup> Meanwhile, the receding contact angle was measured to be (9 ± 3)° within the hydrophilic spots on the substrate and the CAH to be (8 ± 4)° in the hydrophobic regions. All advancing/receding contact angles and the CAH for the distinct regions are summarized in **Table 1**.

### 2.2.3. Substrate Robustness to Various Treatments

The substrate was subject to acidic, basic, and thermal treatments in order to test the durability of the patterning. We found that droplet arrays continued to successfully form on substrates that had been submerged for 1 week in an aqueous environment of either pH = 0.3 or pH = 11.9 (Figure S12, Supporting Information). The FDTs coating also exhibited great thermal stability, withstanding 300 °C for (8 ± 2) h, in line with published results,<sup>[22]</sup> which further increases the versatility of the droplet array platform (see Section S3.2 in the Supporting Information for test details).

### 2.2.4. Producing Gradient Droplet Arrays

As the withdrawal velocity affects the entrained droplet height, arrays featuring drops with fixed footprints and a gradient in heights were achieved by accelerating the biphilic substrate during extraction from the liquid reservoir. The concept is schematically presented in Figure 1b, where the biphilic substrate is necessary for the production of droplet arrays and the nonuniform withdrawal speed is key to generating droplets of different heights on a regular array of identical hydrophilic spots. The photograph in Figure 1b depicts a typical gradient droplet array prepared in this way.

Two different setups were built to vary the velocity of the substrate as it emerged from the reservoir, with details provided in Sections S2.1 and S2.4 in the Supporting Information.

Whether to use linear (Figure 1c, left) or rotational (Figure 1c, right) dip-coating was determined by the size of the hydrophilic spots on the substrate. For small (≤1 mm diameter) hydrophilic spots on the substrate, we used linear acceleration dip-coating, in which the substrate was withdrawn from the reservoir at a fixed angle but progressively increasing speed (Figure 1c, left). Rotational dip-coating, in which the substrate was rotated out of the reservoir (Figure 1c, right), was employed for substrates featuring larger hydrophilic footprints, as this setup takes advantage of both the speed and the angular dependency, thereby enabling steeper volume gradients and thus larger height ranges. It is noteworthy that the rotational setup is mostly applicable for larger droplet arrays as the shift in location  $x$  throughout the array should be significant compared to the optional offset from the rotational axis,  $x_0$  (indicated on **Figure 2a-i**), to create noticeable gradients ( $x_0$  was on the mm to cm-scale due to dimensional constraints of LEGO bricks (LEGO, Billund, Denmark), which was used for building the rotational dip-coating setup). In the case of constant linear acceleration,  $a$ , the withdrawal speed scales with the square root of traveled distance,  $u \sim \sqrt{ax}$ . For rotational extraction at a constant angular velocity,  $\omega$ , defined at the hinge/pivot (the axis of rotation), the withdrawal speed for a droplet at position  $x$  (the projected distance from the hinge) is:  $u(x) = x_0\omega[1 + (x/x_0)^2]$ . We note that near the  $x_0 = 0$  limit, this expression tends to infinity and is not valid.

## 2.3. Droplet Imaging and Characterization

Three different imaging techniques were employed to either 1) visualize the droplet formation process in real-time and inform theoretical analysis or 2) characterize the resulting droplet arrays. Time-lapse imaging of the substrate as it was withdrawn from the reservoir allowed us to gain mechanistic understanding, as described in Section 2.3.1 and illustrated in Figure 2a. We extracted the local withdrawal speed to calculate the capillary number (data and model provided in Section S2.3, Supporting Information), which was then employed to compare with theory, as discussed in Section 3. To characterize the resulting droplet arrays, we measured the heights of the droplets using one of two experimental methods, depending on the droplet size: side-view imaging was sufficient for 1D arrays of larger droplets, while micron-size droplets and 2D arrays required a more nuanced top-view imaging technique, both of which are discussed below (Section 2.3.2 and Figure 2b,c).

### 2.3.1. Visualizing the Droplet Formation Process

The droplet formation process was visualized using time-lapse imaging with the camera positioned directly above the substrate where the substrate exits the reservoir (Figure 2a-i). The resulting camera view is shown schematically in Figure 2a-ii to clarify the photographs in Figure 2a-iii. When submerged, the superhydrophobic regions of the substrate appeared silvery due to the thin layer of air (plastron) that surrounds it.<sup>[23]</sup> This indicates that the liquid is in the Cassie-Baxter state (air filling the surface nanostructure under the drop), which

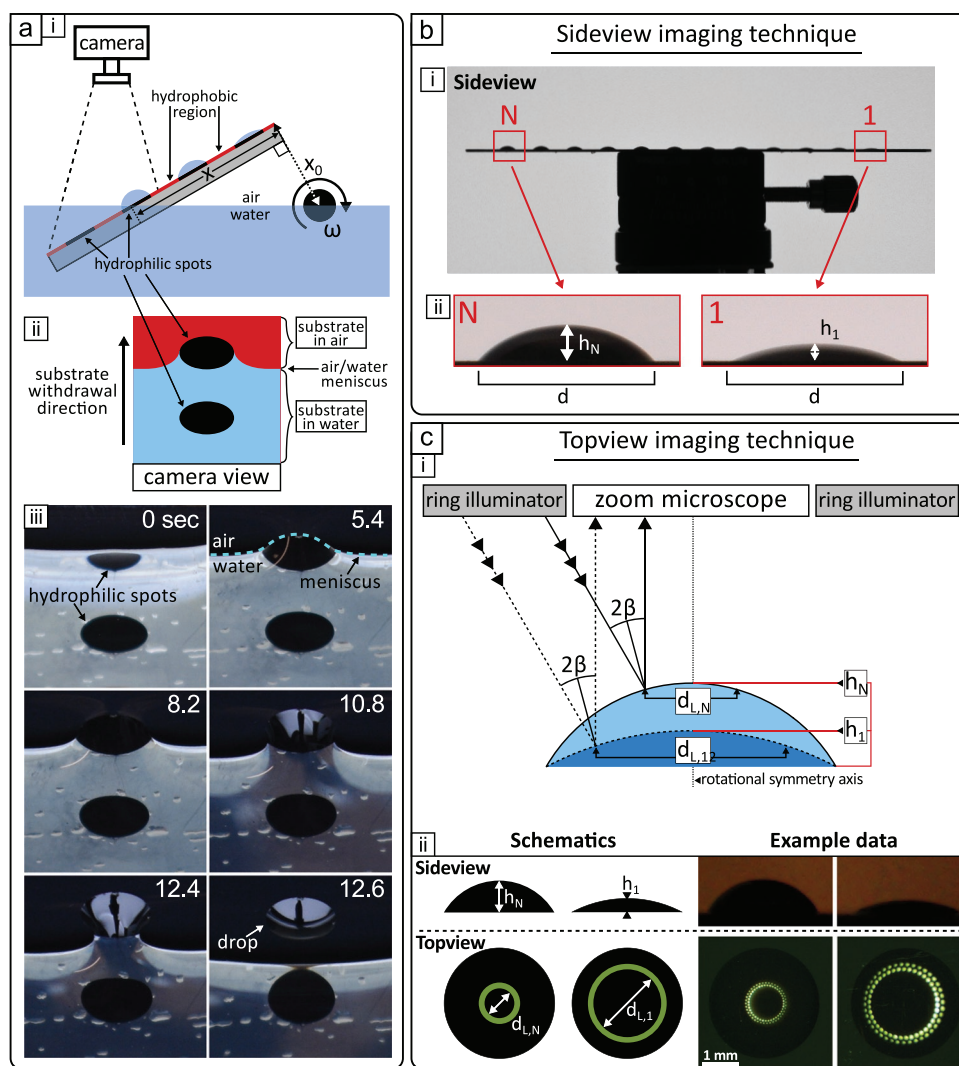


**Figure 2.** Imaging systems to visualize droplet formation and determine their heights. a) Time-lapse imaging of droplet formation process. i) Schematic of the rotational dip-coating setup. The camera is positioned directly above the location of the air–water interface so that droplets can be visualized as they emerge from the reservoir. ii) Schematic of the camera-view. iii) Still images from a time-lapse recording of droplet formation (5 mm base diameter). b) Side-view imaging to determine the heights for millimeter-sized droplets. i) Photograph of gradient droplet array on a stage. ii) Zoom-in on the largest ( $N$ ) and smallest ( $1$ ) droplets with  $h_N$ ,  $h_1$  indicating the measured heights ( $d = 3$  mm;  $N = 12$  here). c) Top-view imaging technique employed to determine the heights of micrometer-sized droplets. i) Schematic showing how the light from a ring illuminator is reflected in two droplets (dark blue droplet has a smaller height  $h_1$  than the light blue droplet with height  $h_N$ , leading to a larger reflected diameter for the smaller drop:  $d_{L,1} > d_{L,N}$ ). ii) Schematics (left) and example data (right) showing that droplets with smaller height result in larger reflected diameters; here the droplet footprint diameter was 3 mm.

is generally associated with lower adhesion and CAH than the Wenzel state (liquid filling the nanostructure). Meanwhile, the hydrophilic spots appeared super black,<sup>[24]</sup> which is caused by a combination of antireflective and absorbing properties of the nanostructured substrate combined with the liquid being in the Wenzel state. The part of the substrate extracted from the reservoir appeared black as well on the camera, again due to the antireflective properties of the nanostructure on the absorbing silicon substrate. Deformation of the liquid meniscus as one hydrophilic region (black circle) emerged from the reservoir can be observed in the still frames acquired with time-lapse imaging. The speed experienced by the individual droplet as it separated from the reservoir, i.e., the withdrawal

speed (Figure S6, Supporting Information), was approximated as the droplet array period (two times the droplet base diameter) divided by the time difference between extraction of the current droplet and its predecessor. The speed was further used to determine the capillary number for each withdrawn droplet (used in Section 3.2).

### 2.3.2. Extracting Droplet Heights

Since the droplet footprints are fixed, droplet height is a sufficient descriptor for droplet size. Two different strategies were used to characterize droplet heights. For 1D arrays of

millimeter-sized droplets, the heights were relatively straightforward to extract using a side-view imaging setup (Figure 2b). Here, the coated substrate was placed on a level stage immediately following completion of the dip-coating procedure and imaged from the side at a resolution of 15  $\mu\text{m pixel}^{-1}$ . The height was determined using a custom-written *MATLAB* script to 1) detect the substrate and calculate its tilt angle, 2) align the substrate to horizontal via image rotation, 3) crop the image, 4) identify the droplets and their positions, and, finally, 5) determine the heights of the droplets using a built-in standard deviation filter (see Figure S4 in the Supporting Information for details of the height analysis procedure, including a visualization). We note that in our experiment, we had a detection limit of  $\approx 0.2$  mm for resolving the droplet heights, determined by the observed discrepancy between the computer-aided image analysis and visual inspection of the images.

Side-view imaging was not an option for the 2D arrays of smaller droplets due to limitations of optical resolution, shadowing effects, and evaporation. Thus, we developed a top-view imaging technique to simultaneously interrogate the entire 2D array, based on a method used by Campbell, Allain, and Langmuir for single droplet characterization.<sup>[25–27]</sup> In our case, a ring-shaped light source illuminated the array from above (Figure 2c-i) and droplet heights were calculated from the diameter of the reflection using Equation (1) (see Figures S8–S11 in the Supporting Information for further details on the conversion, analysis procedure, and data with additional sizes)

$$h = \frac{(d_L/d)}{2\sin\beta} \left( 1 - \sqrt{1 - (d_L/d)^2 \sin^2\beta} \right) d \quad (1)$$

Equation (1) is valid for droplet contact angles,  $\theta$ , from  $\beta$  to  $90^\circ$  (because  $d_L/d \in [\sin\beta, 1]$ ), where  $\beta$  is an experimentally determined angle.

Figure 2c provides schematics and example data to illustrate the counterintuitive coupling between droplet height,  $h$ , and ring reflection diameter,  $d_L$ , where larger  $d_L$  corresponds to smaller  $h$ . Because the droplet arrays in all investigated cases were much smaller ( $\approx 0.5$  cm circumscribed circle radius) than the distance to both the light source ( $\approx 9$  cm) and the microscope objective ( $\approx 6$  cm), it was assumed that the reflection was rotationally symmetric throughout the whole array and that the relationship between individual droplet height and reflection diameter did not depend on droplet base diameter. Consequently, larger droplets were used to calibrate the setup; footprint diameters of 2 and 3 mm were chosen to not significantly exceed the capillary length, which for water is 2.7 mm, such that they can be approximated as spherical caps (see Section S2.4, Supporting Information). The imaging resolution here was 6.2  $\mu\text{m pixel}^{-1}$  for arrays with diameters 1000 and 250  $\mu\text{m}$ , and 2.3  $\mu\text{m pixel}^{-1}$  for arrays with diameter  $d = 50$   $\mu\text{m}$ .

## 2.4. Resulting Gradient Arrays

As mentioned above, 1D gradient arrays consisting of millimeter-sized droplets were created using rotational dip-coating, while 2D arrays of micrometer-sized droplets were produced using linear acceleration-mode dip-coating. The dependence of

the droplet size on various parameters related to the dynamics and geometry of the setups was investigated.

### 2.4.1. Gradients for 1D Arrays of Millimeter-Sized Droplets using Rotational Dip-Coating

Rotational dip-coating enables steeper gradients in droplet heights across the substrate, due to variation in both speed and angle, compared to those achievable by linear acceleration. Droplet heights were determined using side-view imaging and the dependence of height on angular velocity was determined by extracting biphilic substrates at different  $\omega$ , Figure 3a (see Figures S4 and S5 in the Supporting Information for analysis details and additional data, respectively). Angular speeds between 0.58 and 78  $^\circ\text{s}^{-1}$  were chosen as these were the minimum and maximum achievable given the gears employed in the setup and the power that could be applied to the motor. We notice that for the largest angular velocity (78  $^\circ\text{s}^{-1}$ , neon green line), the droplet height first increased and then decreased upon moving away from the hinge due to a transition into the high-speed regime (the transition from the low-speed to the high-speed occurs approximately at 16  $\text{cm s}^{-1}$  when the Froude number, effectively the ratio between flow inertia and gravity, is unity).<sup>[14]</sup> The withdrawal speed remained in the low-speed regime for all other tested angular velocities, showing an expected increase in droplet height with increasing  $\omega$ . Likewise, for fixed  $\omega$ , height increased monotonically for droplets further from the hinge as the extraction speed progressively increased. Here, we produced droplets with contact angles up to  $\approx 45^\circ$ , but a larger contact angle should be possible to achieve, as we have previously demonstrated the creation of millimeter-sized droplets (5 and 7 mm in droplet base diameter) with contact angles above  $60^\circ$  using nonacceleration-mode dip-coating.<sup>[10]</sup>

### 2.4.2. Gradients for 2D Arrays of Micrometer-Sized Droplets using Linear Acceleration Dip-Coating

The biphilic substrates were rotated  $45^\circ$  relative to the reservoir surface normal and were extracted vertically (such that the gradient in droplet heights was along the diagonal of the substrate; see Figure S7, Supporting Information). The method was shown to apply to a large range of hydrophilic spot sizes on the surface (here demonstrated from 50 to 1000  $\mu\text{m}$ ). The arrays were visualized using the ring illumination method described in Section 2.2.2. Figure 3b-i (top left) schematically depicts the (counterintuitive) correlation between droplet height and ring reflection diameter. The photographs in Figure 3b-i show the ring reflections from droplet arrays produced using three different biphilic substrates, featuring hydrophilic spot diameters of 1000, 250, and 50  $\mu\text{m}$ , labeled on the top left of each array (similar images for base diameters of 100 and 500  $\mu\text{m}$  are provided in Figure S11, Supporting Information).

Figure 3b-ii shows the dependence of droplet height on droplet position (measured in millimeters from the droplet that first emerged from the reservoir) along the diagonal white arrows in Figure 3b-i. The droplet heights were calculated from

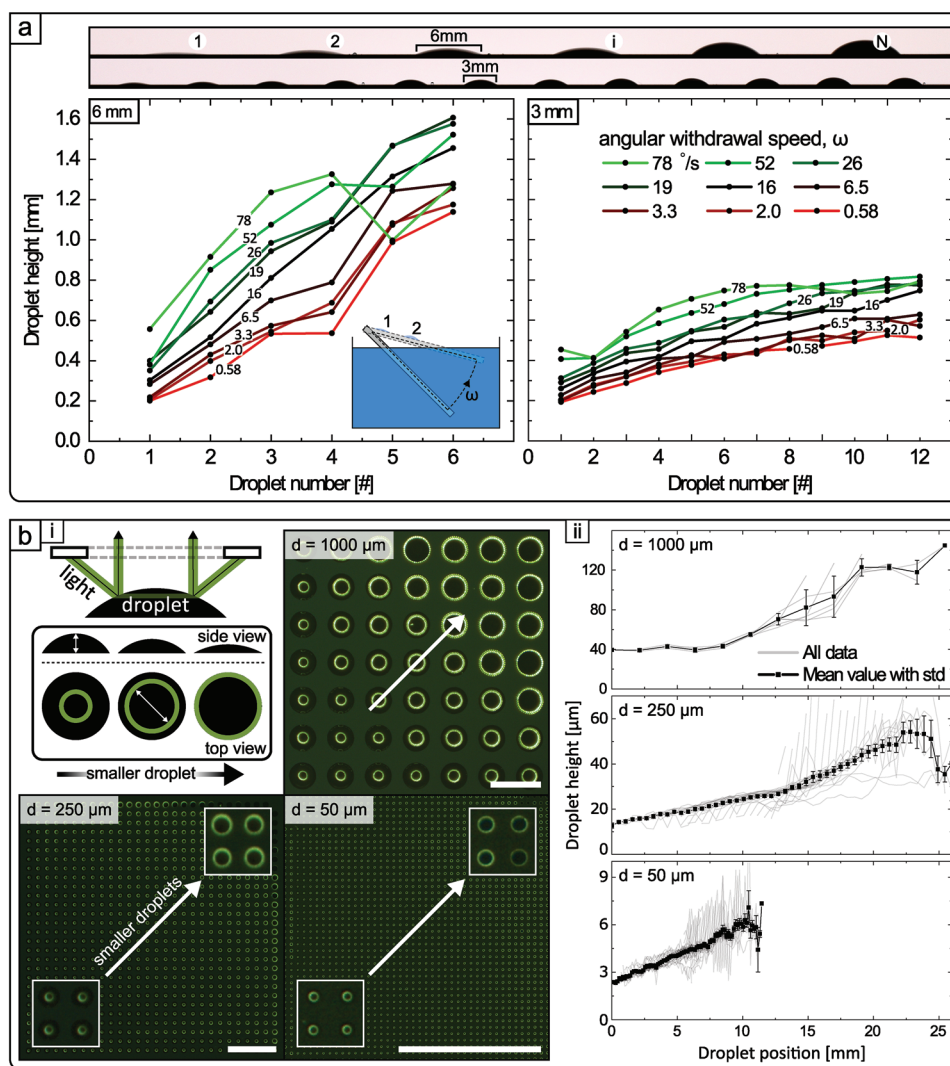


**Figure 3.** Formation of gradients droplet arrays across length scales. a) 1D arrays of droplets produced by rotational dip-coating (bottom-left inset illustrates the process) for two different substrates with drop base diameters of 6 and 3 mm (side-view photographs at the top show drop arrays for angular velocity  $\omega = 3.3^\circ \text{ s}^{-1}$  at the hinge). The distance between neighboring droplets in each array equals the diameter of the hydrophilic spots. Plots show the effects of varying the angular velocity on the droplet height, average for  $n = 5$ . b) 2D microdroplet arrays produced using acceleration-mode linear dip-coating of a substrate in the direction of the array diagonal. Droplet diameters of  $d = 1000$ , 250, and  $50 \mu\text{m}$  are presented with drop-to-drop distances of 400, 125, and  $50 \mu\text{m}$ , respectively. i) Droplet heights were obtained from the diameter of the reflection of the ring illuminator, with the reflection diameter increasing with decreasing droplet contact angle, as in the top left illustration. Insets present zoom-ins from opposing ends of the substrate to help visualize the differences in diameters of the reflected light. The scale bars are 2 mm. The white arrow points from the tallest to the shortest droplets, which—counterintuitively—correspond to the narrowest to widest reflection diameters. ii) The plots show the droplet heights for droplets along the diagonal indicated by the white arrow for each of the arrays. The droplet heights were calculated from the reflection diameters. Data points and error bars are the mean and standard deviation, respectively, as determined for droplets within the same row along the diagonal (up to 7 drops per row for  $d = 1000 \mu\text{m}$ , 28 for  $d = 250 \mu\text{m}$ , and 38 for  $d = 50 \mu\text{m}$ ).

the reflection diameters according to Equation (S1) in the Supporting Information, derived from geometric considerations (see Section S2.4, Supporting Information). This shows that it is indeed possible to create gradients using acceleration-mode dip-coating for 2D arrays of droplets from  $1000 \mu\text{m}$  and down to  $50 \mu\text{m}$ . However, the employed method of *hand-dipping* (Figure S7, Supporting Information) does not allow for quantitatively correlating dip-coating parameters with droplet sizes. Still, we see that it is consistently possible to tune the droplet heights at least a factor of 3, which thereby puts a lower limit

of the accessible range of droplet heights. With an automated experimental setup, it would be possible to conduct a systematic optimization and likely be able to extend this range by tuning the experimental conditions, such as withdrawal acceleration.

### 3. Discussion

For droplet arrays featuring gradients in volumes to be practically useful, it is typically important that there is an appreciable

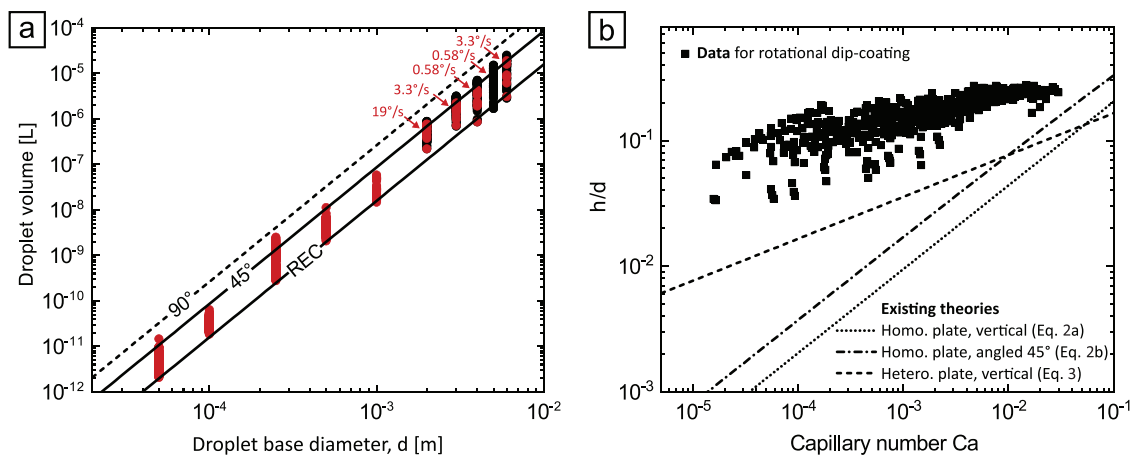


**Figure 4.** Production of gradient arrays at different length scales. a) Summary of the droplet volumes achieved for different droplet base diameters. The red data points exemplify volume variation achieved for a select angular speed (i.e., for the angular speed that gave the largest (relative) droplet variation in the array), while the black data points show the full range of demonstrated droplet volumes by including data from all investigated speeds. The conversion from experimentally measured heights to volume is obtained from ref. [28]. The theoretical diameter–volume relationships for three different droplet contact angles ( $90^\circ$ ,  $45^\circ$ , and  $\text{REC} = 9^\circ$ , the receding contact angle in the hydrophilic region) are denoted in the plot as three parallel lines. b) Experimentally measured height,  $h$ , for millimeter-sized ( $d = 2$  to  $6$  mm) droplets as a function of capillary number,  $Ca$ . The droplets were produced by rotational dip-coating. The lines depict analytical results from existing theories in dip-coating of homogenous (homo) and heterogenous (hetero) plates for vertical and angled ( $45^\circ$ ) withdrawal.

size difference between the smallest and largest droplets within an array formed on a single substrate. The variation in droplet size achievable for a given substrate patterned with a single droplet footprint was assessed experimentally (Section 3.1) and compared to analytical theory (Section 3.2).

### 3.1. Summarizing Effect across Length Scales

Figure 4a shows the spread in droplet volumes for different biphilic substrates, each with a distinct hydrophilic spot diameter, which is indicated on the  $x$ -axis. The  $y$ -axis consists of the droplet volumes, obtained from the measured droplet heights using a spherical cap assumption,  $V = \frac{\pi h}{6} \left( \frac{3}{4}d^2 + h^2 \right)$  where  $d$  is the droplet base diameter and  $h$  is its height.<sup>[28]</sup> Each vertical cluster of points corresponds to data from a single biphilic substrate. Within each cluster, red dots correspond to volume variations across an array withdrawn with dip-coating parameters at the angular velocity that gave the highest spread in droplet volumes for that substrate. Meanwhile, the black dots are additional volumes achieved at other angular velocities for the same substrate, in order to show the full range of droplet volumes achieved for all withdrawal experiments in this study.

To indicate the wide range of droplet contact angles,  $\theta$ , obtained, the theoretical relationship between droplet diameter and volume ( $V = \frac{\pi}{3} (2 + \cos\theta) (1 - \cos\theta)^2 \left( \frac{d}{2 \sin\theta} \right)^3$ , derived from ref. [28] assuming negligible gravity) is plotted for three different droplet contact angles ( $90^\circ$ ,  $45^\circ$ , and  $\text{REC} = 9^\circ$ , the receding contact angle in the hydrophilic region). We observed that the ability to vary volumes via acceleration-mode dip-coating remains significant as the droplet base diameter is decreased, which means that the method likely also works for both smaller and larger footprints than the  $50 \mu\text{m}$  to  $6$  mm range we have tested. This is important because the ability to create gradient arrays in a

parallel manner becomes increasingly more important as droplets are scaled down, due to difficulties creating the droplets via other techniques (such as inkjet printing,<sup>[29]</sup> even when acoustophoretic printing is employed<sup>[30]</sup>) and the large number of droplets makes it time-consuming to produce them drop-by-drop.

### 3.2. Explaining Droplet Size with Analytical Theory

To rationalize the experimental data, and to understand the large spectrum of drop sizes that can be accessed on a single substrate, we applied well-known theories for the thickness of the liquid layer entrained by a solid substrate withdrawn from a liquid bath.<sup>[31–39]</sup> Most studies have been conducted with unstructured, chemically homogenous substrates, where the film thickness scales as  $h \sim Ca^{2/3}$ . Here,  $Ca = \frac{\mu u}{\sigma}$  is the capillary number, which characterizes the relative magnitude of viscous and surface tension forces;  $\sigma$  is the surface tension of the liquid and  $\mu$  is the liquid viscosity. Also importantly, Krechetnikov and Homsy showed, by looking at the effect of roughness on the drag flow, that for small roughness features ( $r/h \ll 1$ ), the  $2/3$  thickness dependence is preserved.<sup>[40]</sup>

Landau, Levich, and Deryagin were the first to calculate the thickness of a film entrained on an infinite flat plate withdrawn vertically at the speed  $u$  from a reservoir.<sup>[31,32]</sup> Assuming that gravitational drainage is negligible and that the coating thickness on a homogenous surface is established by a balance between viscous and capillary forces, they found

$$h = 0.946 \ell_c Ca^{2/3} \quad (2a)$$

where  $Ca \ll 1$  and  $\ell_c = \left( \frac{\sigma}{\rho g} \right)^{1/2}$  is the capillary length;  $\rho$  is the liquid density and  $g$  is the acceleration due to gravity. For a homogenous plate dragged out of a liquid reservoir at an angle  $\alpha$ , Wilson<sup>[35]</sup> showed that the film thickness is given by

$$h = \ell_c \text{Ca}^{\frac{1}{2}} \frac{1}{(1 - \sin \alpha)^{\frac{1}{2}}} \left( 0.946 \text{Ca}^{\frac{1}{6}} - \frac{0.107 \cos \alpha}{1 - \sin \alpha} \text{Ca}^{\frac{1}{2}} + \dots \right) \quad (2b)$$

For patterned surfaces, with wetting areas surrounded by nonwetting regions, experiments have demonstrated that the thickness  $h$  of the entrained film is significantly different from that on homogenous surfaces, due to the lateral confinement of the liquid which is not accounted for in Equations (2a) and (2b).<sup>[9]</sup> For vertically oriented hydrophilic strips of width  $d$ , Darhuber et al.<sup>[9]</sup> and Davis<sup>[41]</sup> showed that the film thickness scales as

$$h = Kd\text{Ca}^{1/3} \quad (3)$$

where  $K$  is a geometry-dependent numerical constant ( $K = 0.356$  for vertical withdrawal). From this scaling relationship, we see that the droplet height is expected to increase with viscosity and decrease with surface tension, which is noteworthy as researchers transition to applications using solvents other than water, or where solutes may decrease the surface tension.

We observe reasonable qualitative agreement between our rotational dip-coating experiments and the capillary number dependence in Equation (3) (Figure 4b; see Figure S6 in the Supporting Information for the determination of withdrawal speed, which was based on the time-lapse imaging presented in Figure 2a). However, it is important to emphasize that the rotational motion, with its orthogonal velocity component, is expected to further increase the film thickness relative to both Equations (2) and (3), explaining the quantitative discrepancy between experiments and the theoretical analysis. Furthermore, Darhuber et al. found that hydrophilic regions interact to increase entrained volume when their separation is smaller than the capillary length.<sup>[9]</sup> When applying Equation (3) to our experiments on hydrophilic circles, it is important to note that the film thickness  $h$  is a function of the capillary number  $\text{Ca}$ , and hence the characteristic extraction speed  $u$ . Because the distance  $x$  to the hinge varies across the sample, the withdrawal speed  $u \sim \omega x^2$ , where  $\omega$  is the frequency of rotation, also differs. This allows us to vary the film thickness across the sample because the local capillary numbers differ. Thus, our experiments complement constant-speed film deposition on chemically patterned substrates (e.g., Brasjen et al.<sup>[6]</sup>) by substantially expanding the range of accessible film thicknesses on each substrate.

### 3.3. Future Opportunities

Gradient droplet array characteristics that can be tuned using these methods are the minimum and maximum droplet heights, the steepness of the gradient, and the monotonicity in the droplet height. Here, we studied the possibility to design these aspects by varying the linear and angular velocities of the substrate. Multiple other opportunities to tune the gradient exist, such as hydrophilic island distribution on the substrate. The distribution matters as neighboring spots distort the local reservoir meniscus, which in turn affects the sizes of entrained droplets. Neighboring droplets, orthogonal to the withdrawal direction, interact to increase entrained droplet sizes if their

separation is smaller than the capillary length (for water  $\approx 2.7$  mm).<sup>[9]</sup> For neighbors along the withdrawal direction, they can interact if meniscus deformation relaxation time is comparable to or longer than the period between their formations. Likewise, the meniscus is typically deformed at the edge of the substrate being withdrawn; the distance to the substrate edge needed to neglect edge effects is one capillary length or larger. Finally, it may also be possible to tune the gradient characteristics by altering the evaporation dynamics, such as through variations in the geometrical configuration (e.g., using a smaller reservoir such that the substrate edges are close to the reservoir edges, affecting the meniscus) or environment (e.g., humidity, temperature) of the dip-coating setup, as has been demonstrated in the formation of films with gradients in thickness.<sup>[42]</sup>

While dip-coating of our biphilic substrate led to droplet array formation for all investigated speeds, it presumably does not happen for all speeds. For chemically homogenous partially wetting substrates (i.e., also both our hydrophilic and hydrophobic regions when considered separately), there is a wettability-dependent critical speed above which forced wetting sets in and results in film formation upon dip-coating; below this critical speed the liquid reservoir simply recedes from the substrate, leaving it dry.<sup>[43]</sup> The consequence for biphilic substrates is a functional range of withdrawal speeds within which a film forms in the hydrophilic regions (defines the minimum speed) while none forms in the hydrophobic ones (defines the maximum speed). However, our ability to predict this functional range is limited as existing theories focus on structurally smooth and chemically homogenous substrates.<sup>[44–46]</sup> In fact, roughness affects the critical speed<sup>[47,48]</sup> and our chemical pattern distorts the triple line, which likely also leads to deviation from existing models. Future experiments and models describing the critical speed as a function of surface roughness and chemical heterogeneity are essential to predicting minimum and maximum heights of withdrawn droplets. In turn, this will improve opportunities to tailor the array gradients to specific applications.

A potential drawback of dip-coating, in general, is the large reservoir volume needed. Fortunately, since only the liquid near the reservoir surface is involved in droplet formation, one way to mitigate this may be to support the deposition liquid above an immiscible liquid (a “dummy phase”),<sup>[49]</sup> especially useful if the deposition liquid is expensive, rare, or time-evolving, e.g., high-purity products or biological materials. For sub-millimeter samples with reservoir sizes small enough for capillary forces to dominate gravity, we also envision that the reservoir could be supported midair via capillary forces.

Finally, by combining multiple gradients, combinatorial chemistry assays can be more readily performed.<sup>[50–52]</sup> One way to achieve this is to use a two-step deposition method similar to the multistep method employed by Faustini et al. to create a continuous functionality gradient.<sup>[11]</sup> In this process, a 2D array with a 1D gradient (similar to those of Figure 3b) can be formed by acceleration-mode dip-coating in a reservoir containing a substance A. The solvent is then allowed to evaporate in order to translate the volume gradient to a gradient in surface concentration.<sup>[53]</sup> This procedure is repeated with another substance B, with the substrate rotated 90° to its original orientation so that the second gradient is orthogonal to the first. Another approach

is the sandwiching method in which two 2D droplet arrays, each with a 1D gradient like in the previous case, on separate substrates are connected face-to-face, oriented such that the gradient directions are orthogonal to one another.<sup>[54]</sup> The first method allows for fast formation of screening arrays, while the second preserves the liquid environment, which is crucial for cell culturing and can be utilized for screening a variety of chemical and biochemical reactions.<sup>[55,56]</sup>

## 4. Conclusion

Using rotational and linear dip-coating setups in acceleration-mode, we unlocked fast formation of gradient droplet arrays with footprints ranging from millimeters to micrometers. Rotational dip-coating was used for 1D arrays of millimeter-sized droplets, while linear acceleration dip-coating was used for 2D arrays of micrometer-sized droplets. We created gradients using droplets with base diameters from as large as 6 mm and down to 50  $\mu\text{m}$ , demonstrating that the method is applicable to droplet volumes spanning more than six orders of magnitude. Within an array, droplet volumes spanned a factor of 3 to 9 depending on the droplet base diameter. The ability to tune the droplet volume is expected to continue at even shorter length scales as the effect showed no sign of diminishing for smaller base diameters, a valuable possibility as the droplets become increasingly more challenging and time-consuming to produce using other methods when scaled down. The experimentally measured volume-dependence of the droplets on the withdrawal speed exhibits a similar power-law dependence as expected from theoretical considerations of chemically heterogeneous substrates. However, the absolute sizes of our droplets were larger than predicted, the exact cause for which remains unknown. The technique is easily compatible with digital droplet array sandwiching, which enables the fast formation of 2D combinatorial chemistry arrays. For the future, we envision combining reconfigurable substrates with acceleration-mode dip-coating to increase versatility even further.

## 5. Experimental Section

In brief, the biphilic substrates were fabricated from 4" Si wafers via first employing a self-masking RIE, with a mixture of sulfur hexafluoride and oxygen gases,<sup>[15]</sup> (Pegasus D-RIE, STS, U.K.) to create nanoroughness followed by a photolithographic process (Figure S1 in the Supporting Information shows mask designs). A monolayer of FDTs was then self-assembled in a molecular vapor deposition system (MVD 100, MST, USA) followed by an acetone lift-off process (see Section S1.1 in the Supporting Information for details). Wettability was characterized using the deflation droplet method as the liquid withdrawal properties were determined for the droplet retention (Attension Theta Optical Tensiometer equipped with a high-speed camera (Motion Xtra N3 with Navitar, IDT)).<sup>[57]</sup> The liquid used was 18.2 M $\Omega$  Milli-Q. For the millimeter-sized droplets, a rotational dip-coater built from LEGO MINDSTORMS was used (Section S2.1 and Figures S2 and S3, Supporting Information) and droplet sizes were characterized with a Nikon D5600 camera using a disassembled computer monitor for the backlight. For the micrometer-sized droplets, the withdrawal was performed by hand (Figure S7, Supporting Information) and characterized by taking top-view images with a reflected light microscope (Zeiss Axio Zoom.V16, Zeiss, Germany) (Section S2.4, Supporting Information). For the 100 and 50  $\mu\text{m}$  droplets,

the substrates were positioned on a dry-ice-chilled copper plate within 2 s after dipping to prevent significant evaporation-induced volume changes. Additional experimental details can be found in the Supporting Information.

**Statistical Analysis:** Figure 1a-ii, contact angle measurements were performed with  $n = 3$ . Figure 1a-iii, SEM micrograph was analyzed manually in ImageJ. Figure 3a, each rotational speed was repeated five times and side-view images analyzed using custom-written scripts in MATLAB 2017b; outliers were preserved despite their cause being known as edge effects from the substrate. Same software was applied to analyze top-view images in Figure 3b with custom-written scripts. Data were visualized and fitted in Origin pro 2021.

## Supporting Information

Supporting Information is available from the Wiley Online Library or from the author.

## Acknowledgements

The financial support from the Danish National Research Foundation (DNRF122), Villum Foundation (grant no. 9301) for Intelligent Drug Delivery and Sensing Using Microcontainers and Nanomechanics (IDUN), and the Novo Nordisk Foundation (NNF17OC0026910)—Microstructures, microbiota and oral delivery (MIMIO) is acknowledged. J.A. and A.V.S. were supported by Harvard University Materials Research Science and Engineering Center (MRSEC) under Award No. DMR-2011754. N.K.M. was supported by an Excellence Ph.D. Scholarship from DTU Health Tech. Dr. Michael Aizenberg is thanked for his comments, and valuable inputs from Rajendra Prasad Shukla, Inhat Chyshankou, Anjali Achazhiyath Edathil, Aakil Lalwani, and En Te Hwu are acknowledged.

## Conflict of Interest

The authors declare no conflict of interest.

## Data Availability Statement

The data that support the findings of this study are available from the corresponding author upon reasonable request.

## Keywords

biphilic surfaces, combinatorial chemistry, droplet microarray technology, high-throughput screening, parallelization of experiments

Received: March 24, 2022

Revised: May 6, 2022

Published online: July 6, 2022

- [1] E. Ueda, P. A. Levkin, *Adv. Mater.* **2013**, 25, 1234.
- [2] W. Feng, E. Ueda, P. A. Levkin, *Adv. Mater.* **2018**, 30, 1706111.
- [3] N. K. Mandsberg, *Adv. Mater. Interfaces* **2021**, 8, 2100815.
- [4] A. Toppi, L. L. Busk, H. Hu, A. A. Dogan, A. Jönsson, R. J. Taboryski, M. Dufva, *ACS Appl. Mater. Interfaces* **2021**, 13, 43914.
- [5] W. Lei, K. Demir, J. Overhage, M. Grunze, T. Schwartz, P. A. Levkin, *Adv. Biosyst.* **2020**, 4, 2000073.

- [6] B. J. Brasjen, H. M. J. M. Wedershoven, A. W. van Cuijk, A. A. Darhuber, *Chem. Eng. Sci.* **2017**, *158*, 340.
- [7] B. J. Brasjen, A. W. van Cuijk, A. A. Darhuber, *Chem. Eng. Process.* **2011**, *50*, 565.
- [8] M. A. C. van Gestel, B. He, A. A. Darhuber, *Chem. Eng. Sci.* **2020**, *227*, 115832.
- [9] A. a. Darhuber, S. M. Troian, J. M. Davis, S. M. Miller, S. Wagner, *J. Appl. Phys.* **2000**, *88*, 5119.
- [10] N. K. Mandsberg, O. Hansen, R. Taboryski, *Sci. Rep.* **2017**, *7*, 12794.
- [11] M. Faustini, D. R. Ceratti, B. Louis, M. Boudot, P. A. Albouy, C. Boissière, D. Grosso, *ACS Appl. Mater. Interfaces* **2014**, *6*, 17102.
- [12] R. L. Davis, S. Jayaraman, P. M. Chaikin, R. A. Register, *Langmuir* **2014**, *30*, 5637.
- [13] H. A. Biebuyck, G. M. Whitesides, *Langmuir* **1994**, *10*, 2790.
- [14] A. De Ryck, D. Quéré, *J. Colloid Interface Sci.* **1998**, *203*, 278.
- [15] L. Schneider, M. Laustsen, N. Mandsberg, R. Taboryski, *Sci. Rep.* **2016**, *6*, 21400.
- [16] J. J. Bikerman, *J. Colloid Sci.* **1950**, *5*, 349.
- [17] K. Kawasaki, *J. Colloid Sci.* **1960**, *15*, 402.
- [18] C. G. L. Fumridge, *J. Colloid Sci.* **1962**, *17*, 309.
- [19] N. K. Mandsberg, R. Taboryski, *Surf. Topogr.: Metrol. Prop.* **2017**, *5*, 024001.
- [20] L. Feng, Y. Zhang, J. Xi, Y. Zhu, N. Wang, F. Xia, L. Jiang, *Langmuir* **2008**, *24*, 4114.
- [21] B. Bhushan, M. Nosonovsky, *Philos. Trans. R. Soc., A* **2010**, *368*, 4713.
- [22] Y. X. Zhuang, O. Hansen, T. Knieling, C. Wang, P. Rombach, W. Lang, W. Benecke, M. Kehlenbeck, J. Koblitz, *J. Microeng. Microeng.* **2006**, *16*, 2259.
- [23] N. J. Shirtcliffe, G. McHale, M. I. Newton, C. C. Perry, F. B. Pyatt, *Appl. Phys. Lett.* **2006**, *89*, 10.
- [24] D. E. McCoy, V. E. McCoy, N. K. Mandsberg, A. V. Shneidman, J. Aizenberg, R. O. Prum, D. Haig, *Proc. R. Soc. B* **2019**, *286*, 20190589.
- [25] J. M. Campbell, H. K. Christenson, *ACS Appl. Mater. Interfaces* **2018**, *10*, 16893.
- [26] C. Allain, D. Ausserre, F. Rondelez, *J. Colloid Interface Sci.* **1984**, *107*, 5.
- [27] I. Langmuir, V. J. Schaefer, *J. Am. Chem. Soc.* **1937**, *59*, 2400.
- [28] A. D. Polyani, A. V. Manzhirov, *Mathematics for Engineers and Physicists*, Chapman and Hall/CRC, London/Boca Raton, FL **2006**.
- [29] N. K. Mandsberg, J. Højgaard, S. S. Joshi, L. H. Nielsen, A. Boisen, E. Te Hwu, *ACS Omega* **2021**, *6*, 7786.
- [30] D. Foresti, K. T. Kroll, R. Amissah, F. Sillani, K. A. Homan, D. Poulikakos, J. A. Lewis, *Sci. Adv.* **2018**, *4*, eaat1659.
- [31] B. Landau, L. Levich, *Acta Physicochim. URSS* **1942**, *17*, 42.
- [32] B. M. Deryagin, S. M. Levi, *Film Coating Theory*, Focal, New York, **1964**.
- [33] D. A. White, J. A. Tallmadge, *Chem. Eng. Sci.* **1965**, *20*, 33.
- [34] C. Y. Lee, J. A. Tallmadge, *AIChE J.* **1972**, *18*, 1077.
- [35] S. D. R. Wilson, *J. Eng. Math.* **1982**, *16*, 209.
- [36] O. Réglat, R. Labrie, P. A. Tanguy, *J. Comput. Phys.* **1993**, *109*, 238.
- [37] P. R. Schunk, A. J. Hurd, C. J. Brinker, in *Liquid Film Coating* (Eds: S. F. Kistler, P. M. Schweizer), Springer, Dordrecht **1997**, pp. 673–708.
- [38] D. Quéré, *Annu. Rev. Fluid Mech.* **1999**, *31*, 347.
- [39] S. J. Weinstein, K. J. Ruschak, *Annu. Rev. Fluid Mech.* **2004**, *36*, 29.
- [40] R. Krechetnikov, G. M. Homsy, *Phys. Fluids* **2005**, *17*, 102108.
- [41] J. M. Davis, *Phys. Fluids* **2005**, *17*, 038101.
- [42] E. Bindini, G. Naudin, M. Faustini, D. Grosso, C. Boissière, *J. Phys. Chem. C* **2017**, *121*, 14572.
- [43] R. V. Sedev, J. G. Petrov, *Colloids Surf.* **1991**, *53*, 147.
- [44] T. Shing Chan, T. Gueudré, J. H. Snoeijer, *Phys. Fluids* **2011**, *23*, 112103.
- [45] P. Gao, L. Li, J. J. Feng, H. Ding, X. Y. Lu, *J. Fluid Mech.* **2016**, *791*, 358.
- [46] T. S. Chan, J. H. Snoeijer, J. Eggers, *Phys. Fluids* **2012**, *24*, 072104.
- [47] R. Golestanian, E. Raphaël, *Europhys. Lett.* **2001**, *55*, 228.
- [48] J. Eggers, *Phys. Rev. Lett.* **2004**, *93*, 094502.
- [49] D. R. Ceratti, B. Louis, X. Paquez, M. Faustini, D. Grosso, *Adv. Mater.* **2015**, *27*, 4958.
- [50] A. Kulesa, J. Kehe, J. E. Hurtado, P. Tawde, P. C. Blainey, *Proc. Natl. Acad. Sci. USA* **2018**, *115*, 6685.
- [51] M. Benz, A. Asperger, M. Hamester, A. Welle, S. Heissler, P. A. Levkin, *Nat. Commun.* **2020**, *11*, 5391.
- [52] W. Lei, K. Demir, J. Overhage, M. Grunze, T. Schwartz, P. A. Levkin, *Adv. Biosyst.* **2020**, *4*, 2000073.
- [53] D. Qin, Y. Xia, B. Xu, H. Yang, C. Zhu, G. M. Whitesides, *Adv. Mater.* **1999**, *11*, 1433.
- [54] A. A. Popova, S. M. Schillo, K. Demir, E. Ueda, A. Nesterov-Mueller, P. A. Levkin, *Adv. Mater.* **2015**, *27*, 5217.
- [55] G. Jogia, T. Tronser, A. Popova, P. Levkin, *Microarrays* **2016**, *5*, 28.
- [56] A. A. Popova, T. Tronser, K. Demir, P. Haitz, K. Kuodyte, V. Starkuviene, P. Wajda, P. A. Levkin, *Small* **2019**, *15*, 1901299.
- [57] T. Huhtamäki, X. Tian, J. T. Korhonen, R. H. A. Ras, *Nat. Protoc.* **2018**, *13*, 1521.